Reactive sintering and particle morphology control of β″-alumina-based water purification filters

著者別名	鈴木 義和
journal or publication title	Journal of materials science
volume	53
number	2
page range	1005-1013
year	2018-01
権利	(C) Springer Science+Business Media, LLC 2017 This is a post-peer-review, pre-copyedit version of an article published in Journal of materials science . The final authenticated version is available online at: http://dx.doi.org/10.1007/s10853-017-1599-z”
URL	http://hdl.handle.net/2241/00149230

doi: 10.1007/s10853-017-1599-z

J. Mater. Sci.
Revision: September 8, 2017

Reactive sintering and particle morphology control of β"-alumina based water-purification filters

Kazuki Fukui [a], Yoshikazu Suzuki [a,b*]

[a] Graduate School of Pure and Applied Sciences, University of Tsukuba, 1-1-1 Tennodai, Tsukuba, Ibaraki, 305-8573, Japan

[b] Faculty of Pure and Applied Sciences, University of Tsukuba, 1-1-1 Tennodai, Tsukuba, Ibaraki, 305-8573, Japan

Abstract

This paper reports on the preparation of porous membranes consisting of plate-like β"-alumina grains and the evaluation for microfiltration properties. Porous β"-alumina-based ceramics were prepared by the solid-state reactive sintering of Na_2CO_3 and α-Al_2O_3 at 1100-1300 °C. To study the effect of impurities in the starting powder mixtures, LiF-doped membranes were also prepared. As for the water filtration test, the turbidity before and after the vacuum filtration was measured using sintered porous membranes. To simulate bacteria-contaminated water, a suspension of a commercial boehmite powder (D_{50} = 0.7 μm) in distilled water was used. The non-doped samples sintered at 1200 °C was composed of β"-alumina (84 wt.%) and β-alumina (16 wt.%) grains, and showed a good microfiltration performance; the turbidities before and after filtration were 894.4 NTU and 1.46 NTU, respectively.

Keywords

β"-alumina; β-alumina; $NaAlO_2$; Porous ceramics; Water purification; Microfiltration

[*] Corresponding author:
Division of Materials Science, Faculty of Pure and Applied Sciences,
University of Tsukuba, Ibaraki 305-8573, Japan (phone: +81-29-853-5026)
E-mail: suzuki@ims.tsukuba.ac.jp (Y. Suzuki)

Introduction

β"-alumina (ca. $Na_2O{\cdot}5.33Al_2O_3$~$Na_2O{\cdot}6.5Al_2O_3$, ideally $Na_2O{\cdot}5.33Al_2O_3$) and β-alumina (ca. $Na_2O{\cdot}8.1Al_2O_3$~$Na_2O{\cdot}9.5Al_2O_3$, ideally $Na_2O{\cdot}11Al_2O_3$) have high Na-ion conductivity [1,2], and they have mainly been studied as ion conductors mainly in sodium ion batteries [3-6]. They are also studied for conducting films [7], gas sensors [8,9], high-k gate layer for transparent electronics [10,11] and thermoelectric conversion material [12,13]. The space groups of β"- and β-alumina are $R\bar{3}m$ (166) and $P6_3/mmc$ (194), respectively [14-16], and thus, they idiomorphically grow into hexagonally-shaped plate-like grains [17,18]. It is expected that these plate-like grain morphologies can be used for other applications, such as solid lubricant and catalyst support.

To date, commercial porous microfiltration membranes for bacteria removal are mainly made of polymers [19-21] and ceramics [22-24]. Ceramics membranes are heat resistant, chemically resistant, reusable, protective for biological deterioration, and thus, they generally have long durability [25,26]. A 3D-network structure, formed by constituent ceramic grains, enables high-quality filtration. However, this complex structure generally causes membrane clogging and decreases filtration rate in practical use. Some studies related to membrane recovery were reported [25,27]. We have recently reported ceramics membrane for water purification filters consisting of pseudobrookite-type Al_2TiO_5 [28] and $MgTi_2O_5$ [29], which are well known for low thermal expansion and high thermal shock resistant ceramics. Although anisotropic *rod-like* grains effectively worked during filtration, the filtration-rate was not sufficient for practical uses, i.e. ~6 mL/min using an $MgTi_2O_5$ disc filter with the 22 mm in diameter for the suspension with 0.7 μm filtrate particles [29]. It is note-worthy that water purification filters consisting of $MgAl_2O_4$ spinel *equiaxed* grains were suitable for more precise filtration, but the filtration-rate became much slower (~0.20 mL/min in the similar experimental

conditions of Ref. 29) [30].

Hence, we now focus anisotropic *plate-like* grains for water filtration. This paper reports the preparation of porous membrane of plate-like β"-alumina grains and the evaluation for microfiltration properties with a dead-end setup. Porous ceramics were prepared by solid-state reactive sintering of Na_2CO_3 and α-Al_2O_3. During the reactive sintering, Na_2CO_3 also acted as a pore former similarly to the previous study [31]. Sintering conditions for well-faceted hexagonal grains of β"-alumina were examined. In addition, LiF doping effect to control the phase and microstructure was examined. Fine ceramic particle removal, simulating the bacteria removal in water, was tested with the prepared membranes via the turbidity measurement.

Experimental

Sample preparation

Commercial anhydrous Na_2CO_3 (99.8% purity, Wako Pure Chemicals Industries Ltd., Osaka, Japan) and α-Al_2O_3 (99.99% purity, Taimei Chemicals Co. Ltd., Saitama, Japan) powders were used as starting materials. Na_2CO_3 and Al_2O_3 powders were mixed at 1:5 mole ratio to synthesize β"-alumina, and then wet-ball milled in ethanol with ZrO_2 ball media for 24 h. Note that the mixing ratio of Na:Al = 1:5 used in this study was somewhat Na-rich than the reported composition of β"-alumina (1:5.33 ~ 1:6.5) [1], by taking into account of the vaporization loss of Na_2O during the reactive sintering.

The mixed slurry was dried by evaporator and additionally dried in an oven at 80°C overnight. The mixed powder was then sieving through a 150-mesh (<100 μm) screen. To evaluate an impurity effect (or mineralizer effect via liquid-phase formation), LiF-doped mixed powder was also prepared in the same manner; LiF powder (99.9% purity, Wako Pure Chemical

Industries Ltd.), 0.5 wt.% of the total of anhydrous Na_2CO_3 and α-Al_2O_3 (1:5 mole ratio), was added to a starting mixture prior to the ball milling. Hereafter, these two mixed powders were referred as "non-doped" and "LiF-doped."

For the preliminary phase identification/microstructure evaluation purposes, smaller pellet samples were prepared. The two mixed powders (non-doped and LiF-doped, 1.0 g each) were uniaxially pressed to disk-shaped green bodies (15 mmΦ) at 36 MPa for 1 min. These green bodies were sintered at 1100-1300°C for 2 h with a heating rate of 300°C/h in air. For the water filtration test purposes, larger pellet samples with higher porosity were prepared. The two mixed powders were uniaxially pressed to disk-shaped green bodies (30 mmΦ) at 3 MPa for 1 min, and then sintered at 1200°C for 2 h with heating rate of 300°C/h in air.

Characterization

Component phases of the pulverized samples after sintering were determined by X-ray diffraction (XRD, Cu-Kα, 40 kV, 40 mA, Multiflex, Rigaku, Japan). Fracture surfaces of the samples were observed by SEM (JSM-5600/SV, JEOL). Density and porosity were calculated from sample dimension and mass. The pore-size distribution was determined by mercury intrusion porosimetry (PoreMaster-60-GT, Quantachrome). Washburn equation was used to calculate the pore size, where mercury surface tension is 480 dyne/cm and mercury contact angle is 140° [30].

For the water filtration test, sintered porous membranes (~30 mmΦ) were set in a close contact fixation with rubber packing. The effective filtration area was 22 mm in diameter. **Figure 1** shows the filtration test setup (dead-end type). Since the size of Escherichia coli is ~0.5 μm in diameter and 1-3 μm in length, a suspension of a commercial boehmite powder (D_{50} = 0.7 μm, C_{06}. Taimei Chemicals Co. Ltd) in distilled water was used to simulate

bacteria-contaminated water [29,30]. The turbidity of the initial suspension was 894.4 NTU.

Results and Discussion

Phase identification

Figure 2 shows XRD patterns of reactively sintered samples, and **Table 1** summarizes the phase compositions calculated from the following equations reported by Shen et al. [32]:

$$w^{\beta"} = 2.41I^{\beta"}_{(024)}/(2.41I^{\beta"}_{(024)} + 3.11I^{\beta}_{(012)} + I^{NaAlO_2}_{(120)})$$

$$w^{\beta} = 3.11I^{\beta}_{(012)}/(2.41I^{\beta"}_{(024)} + 3.11I^{\beta}_{(012)} + I^{NaAlO_2}_{(120)})$$

$$w^{NaAlO_2} = I^{NaAlO_2}_{(120)}/(2.41I^{\beta"}_{(024)} + 3.11I^{\beta}_{(012)} + I^{NaAlO_2}_{(120)})$$

For the non-doped samples (Fig. 2(a)), at 1100°C, α-Al_2O_3 (unreacted starting phase) and $NaAlO_2$ (partially reacted intermediate phase) were identified. At 1200°C and 1300°C, β"-alumina (major)/ β-alumina (minor) composites were synthesized.

On the other hand, for the LiF-doped samples (Fig. 2(b)), at 1100°C and 1200°C, major β-alumina and minor $NaAlO_2$ phases were identified. At 1300°C, β-alumina, β"-alumina and $NaAlO_2$ phases were identified. These results suggested that LiF doping stabilized the intermediate β-alumina phase.

Microstructure and pore structure

Figure 3 shows microstructures of the fracture surfaces for non-doped and LiF-doped sintered samples. As for the non-doped samples, at 1100°C (Fig. 3(a)), fine and isotropic grains were mainly observed, which are attributed to unreacted α-Al_2O_3. Some rod-like grains were

also observed, and they might be attributable to $NaAlO_2$ hydrate (i.e., $NaAlO_2$ reacted with atmospheric H_2O) [33]. At 1200°C (Fig. 3(b)), anisotropic plate-like β"- and β-alumina grains formed a card-house 3D network structure. At 1300°C (Fig. 3(c)), sintering of plate-like grains was observed.

As for the LiF-doped samples, at 1100°C (Fig. 3(d)), anisotropic plate-like β-alumina grains start to form (with vestigial particle-like morphology). At 1200°C (Fig. 3(e)), well-developed β-alumina grains of 20-30 μm formed a card-house 3D network structure. At 1300°C (Fig. 3(f)), sintering of plate-like grains also proceeded. For both the non-doped and the LiF-doped systems, card-house structures were formed at 1200°C, but the size and the constitution phases were quite different to each other.

Figure 4 and **Table 2** show the results of mercury porosimetry. In good accordance with the SEM observation [Figs. 3 (b) and 3 (e)], the non-doped and the LiF-doped samples contained smaller and larger pores (median sizes of 0.63 and 5.07 μm), respectively. In addition, the total pore volumes of these samples were 0.198 and 0.477 cm^3, respectively. As is described in the following section, the porosities of two samples calculated from the dimension-mass were almost the same, which suggests the difference of open porosity.

Filtration test

Considering the XRD and SEM results, sintering at 1200°C was adequate for both non-doped and LiF-doped samples. **Table 3** summarizes density, porosity and filtration performance of the porous membranes reactively sintered at 1200°C. Note that the porosity values are estimated from the theoretical densities of β"-alumina (3.321 g/cm^3 [34]), β-alumina (3.258 g/cm^3 [35]) and $NaAlO_2$ (2.754 g/cm^3 [36]) phases. Although the two membranes with or without LiF doping had similar porosity values (~60 %), the filtration results were quite

different to each other (**Fig. 5**). As can be seen in Figs. 3 (b) and 3 (e), the LiF-doped sample was composed of much larger platelets and contained large open pores, which resulted in insufficient removal of fine particles similar to the size of bacteria (see Fig. 5 right).

Figure 6 shows optical microscopy images of the surface morphology of porous membranes. For the non-doped sample, large amount of boehmite particles were accumulated on the surface of the sample (Fig. 6(b)). A small amount of boehmite particles were also observed on the bottom side (Fig. 6(c)). For the LiF-doped sample, boehmite particles were hardly observed on the both sides (Fig. 6 (e) and (f)), which implies that the boehmite particles easily penetrated to the open pores. The fracture surfaces (i.e. internal structures) of samples after the filtration are shown in **Fig. 7**. In the non-doped sample, large amount of boehmite particles were captured in the spaces among β"-alumina platelets. On the contrary, in the LiF-doped sample, a small amount of particles were trapped in the spaces among β-alumina platelets, particularly at the overlapped intersection of platelets.

Phase evolution with/without LiF doping

In this study, as shown in Fig. 2 and Table 1, the non-doped samples consisted of β"- and β-alumina phases at 1200-1300 °C, whereas the LiF-doped samples consisted of β-alumina and $NaAlO_2$ at 1100-1200 °C, and β"-, β-alumina and $NaAlO_2$ at 1300 °C. The difference of phase evolution can be explained by the microstructure development and phase diagram. As can be seen in the Na_2O-Al_2O_3 calculated phase-diagram reported by Besmann and Spear in **Fig. 8** [37], the initial products by the solid-state reaction between Na_2O and Al_2O_3 should be $NaAlO_2$ at Na_2O side and β-alumina ("$Na_2Al_{22}O_{34}$" in Fig. 8) at Al_2O_3 side. For the non-doped sample, β"-alumina ("$Na_2Al_{12}O_{19}$" in Fig. 8) was the main product (with some residual β-alumina with higher thermal stability). For the LiF-doped sample, however, the surface diffusion and

vaporization-condensation during sintering were accelerated with the doping of LiF mineralizer (i.e. liquid-phase formation), and hence, intermediate β-alumina phase was synthesized/stabilized at lower temperatures, which resulted in the remarkable growth of hexagonal plate-like grains. Due to the stabilization of β-alumina phase, the Na-rich intermediate compound ($NaAlO_2$) remained until higher sintering temperatures.

Removal of colloidal particles

From the microstructure observations (Figs. 6 and 7), a filtration model for a porous card-house structure is constructed as illustrated in **Fig. 9**. Firstly, colloidal particles in the suspension enter the open-pores formed by plate-like grains (β" or β-alumina). Then, the particles approach the plate-like grains and move along on the plate-like grain surfaces. The particles are trapped and accumulated in the assembly of the plate-like grains. Thereafter, trapped particles form the cakes, and subsequent particles are continuously removed by them. Considering this model, the assemblies of plate-like grains in the non-doped samples are relatively fine (due to the small plate-like grains), and they effectively capture the colloidal particles. On the other hand, those in the LiF-doped samples are relatively course (due to the large plate-like grains), and they leak out some colloidal particles, resulting in a higher turbidity (Fig. 5 and Table 3) with a slightly higher filtration rate.

Conclusions

In this research, porous membranes mainly composed of plate-like grains were prepared by reactive sintering for the microfiltration. In conclusions:

(1) For the non-doped samples, β"-alumina (major)/ β-alumina (minor) composites were

synthesized at 1200°C and 1300°C. At 1200°C, anisotropic plate-like β"- and β-alumina grains (in several micrometers) formed a card-house 3D network structure. Due to its fine card-house 3D network structure, colloidal particles (~0.7 μm) in a suspension were effectively captured. The turbidities before and after filtration were 894.4 NTU and 1.46 NTU, respectively.

(2) For the LiF-doped samples, major β-alumina and minor $NaAlO_2$ phases were confirmed at 1100°C and 1200°C. The results suggested that the LiF doping stabilized the intermediate β-alumina phase. At 1200°C, well-developed β-alumina grains of 20-30 μm formed a large card-house 3D network structure, which resulted in the insufficient removal of the colloidal particles. The turbidities before and after filtration were 894.4 NTU and 87.38 NTU, respectively.

Throughout this study, controlling a small amount of liquid-forming impurity in the starting powders is quite important to realize the microfiltration.

Acknowledgements

This work was supported by Nippon Sheet Glass Foundation for Materials Science and Engineering. We thank to Prof. Tamotsu Koyano at University of Tsukuba for the use of SEM observation.

References

[1] Tao YFY, Kummer JT (1967) Ion exchange properties of and rates of ionic diffusion in beta-alumina. J Inorg Nucl Chem 29:2453-2466

[2] Yazhenskikh E, Hack E, Müller M (2008) Critical thermodynamic evaluation of oxide systems relevant to fuel ashes and slags Part 2: Alkali oxide–alumina systems. Calphad

30: 397-404.

[3] Kim KK, Mundy JN, Chen WK (1979) Diffusion and ionic conductivity in sodium beta alumina. J Phys Chem Solids 40:743-755

[4] Seevers R, deNuzzio J, Farrington GC, Dunn B (1983) Ion transport in Ca^{2+}, Sr^{2+}, Ba^{2+}, and Pb^{2+} β″ aluminas. J Solid State Chem 50:146-152

[5] Kummer JT (1972) β-Alumina electrolytes. Progr in Solid State Chem 7:141–175

[6] Lu X, Xia G, Lemmon JP., yang Z (2010) Advanced materials for sodium-beta alumina batteries: Status, challenges and perspectives. J Power Sources 195:2431-2442

[7] Li N, Wen Z, Liu Y, Xu X, Lin J, Gu Z (2009) Preparation of Na-beta"-alumina film by tape casting process. J Eur Ceram Soc 29:3031–3037

[8] Vangrunderbeek J, Vandecruys F, Kumer RV (1999) Sensing mechanism of high temperature hydrogen sulphide sensor based on sodium β-alumina. Sens and Actuators B: Chem 56:129-135

[9] Konakov VG, Kharitonov SN, Kurapova OYu, Archakov IYu (2016) High temperature Ag^{+}-β"-alumina in situ sensor for sulfur-containing gases. J Solid State Electrochem 20:1345–1354

[10] Pal BN, Dhar BM, See KC, Katz HE (2009) Solution-deposited sodium beta-alumina gate dielectrics for low-voltage and transparent field-effect transistors. Nature Mater 8: 898-903

[11] Zhang B, Liu Y, Agarwal S, Yeh ML, Katz HE (2011) Structure, sodium ion role, and practical issues for β-alumina as a high-k solution-processed gate layer for transparent and low-voltage electronics. ACS Appl Mater Interfaces 3:4254–4261

[12] Kuwamoto H, Sato H (1981) Measurement of thermoelectric power of β- and β"-alumina. Solid State Ionics 5:187-188

[13] Subasri R, Nafe H, Aldinger F (2002) Thermoelectric power studies on MgO-stabilized β"-alumina. J. Solid State Electrochem 6: 259-264

[14] Bettman M, Peters CR (1969) The crystal structure of $Na_2O{\cdot}MgO{\cdot}5Al_2O_3$ with reference to Na_2O-$5Al_2O_3$ and other isotypal compounds. J Phys Chem 73:1774-1780

[15] Birinie DP (2012) On the structural integrity of the spinel block in the β"-alumina structure. Acta Cryst B 68:118-122

[16] Beevers CA, Ross MAS (1937) The crystal structure of "Beta Alumina" $Na_2O{\cdot}11Al_2O_3$. Z Kristallogr 97:59-66

[17] Ichikawa S, Takahashi T (1994) Initial-stage sintering of β-alumina. J Cerem Soc Jpn 102:5-7

[18] Ushio M (1995) Crystal growth of thin-plate β-alumina by liquid transport. J Mater Sci 30:2981-2988

[19] Ulbricht M (2006) Advanced functional polymer membranes. Polymer 47:2217-2262

[20] Zularisam AW, Ismail AF (2006) Behaviors of natural organic matter in membrane filtration for surface water treatment-a review. Desalination 194:211-231

[21] Shen Y, Zhao W, Xiao K, Huang X (2010) A systematic insight into fouling propensity of soluble microbial products in membrane bioreactors based on hydrophobic interaction and size exclusion. J Membr Sci 346:187-193

[22] Guerra K, Pellegrino J, Drewes JE (2012) Impact of operating conditions on permeate flux and process economics for cross flow ceramic membrane ultrafiltration of surface water. Sep Purif Technol 87:47-53

[23] Verweij H (2003) Ceramic membranes: Morphology and transport. J Mater Sci 38:4677-4695

[24] Vasanth D, Pugazhenthi G, Uppaluri R (2013) Cross-flow microfiltration of oil-in-water

emulsions using low cost ceramic membranes. Desalination 320:86-95

[25] Bartlett M, Bird MR, Howell JA (1995) An experimental study for the development of a qualitative membrane cleaning model. J Membr Sci 105:147-157

[26] Schafer AI, Schwicker U, Fischer MM, Fane AG, Waite TD (2000) Microfiltration of colloids and natural organic matter. J Membr Sci 171:151-172

[27] Lamminen MO, Walker HW, Weavers LK (2004) Mechanisms and factors influencing the ultrasonic cleaning of particle-fouled ceramic membranes. J Membr Sci 237:213-223

[28] Hono T, Inoue N, Morimoto M, Suzuki Y (2013) Reactive sintering and microstructure of uniform, openly porous Al_2TiO_5. J Asian Ceram Soc 1:178-183

[29] Nakagoshi Y, Suzuki Y (2015) Pseudobrookite-type $MgTi_2O_5$ water purification filter with controlled particle morphology. J Asian Ceram Soc 3:334-338

[30] Kamato Y and Suzuki Y (2017) Reactively sintered porous $MgAl_2O_4$ for water-purification filter with controlled particle morphology. Ceram Int 43:14090-14095

[31] Suzuki Y, Suzuki TS, Shinoda Y, Yoshida K (2012) Uniformly porous $MgT_{i2}O_5$ with narrow pore-size distribution: XAFS study, improved in-situ synthesis, and new in-situ surface coating. Adv Eng Mater 14:1134-1138

[32] Shen JL, Howard SA, Liu J, Ownby PD (1992) Quantitative analysis of the crystalline phases in β"-alumina-based solid electrolytes using x-ray powder diffraction. J Am Ceram Soc 75: 52-55

[33] Liu IL, Lin BC, Chen, SY, Shen P (2011) $NaAlO_2$ and γ-Al_2O_3 nanoparticles by pulsed laser ablation in aqueous solution. J. Phys. Chem. C 115: 4994-5002

[34] ICDD-JCPDS PDF no. 82-0462 ($Na_{1.77}Al_{11}O_{17}$)

[35] ICDD-JCPDS PDF no. 79-1560 ($Na_{1.22}Al_{11}O_{17.11}$)

[36] ICDD-JCPDS PDF no. 33-1200 ($NaAlO_2$)

[37] Besmann TM, Spear KE (2002) Thermochemical modeling of oxide glasses. J Am Ceram Soc 85: 2887-2894

Tables

Table 1. Quantitative analysis of reactively sintered samples.

Samples	Sintering temperature (°C)	β''-alumina (wt.%)	β-alumina (wt.%)	$NaAlO_2$ (wt.%)
Non-doped	1200	**84**	**16**	-
	1300	88	12	-
LiF-doped	1100	-	81	19
	1200	-	**84**	**16**
	1300	42	44	14

Table 2 Mercury porosimetry analysis for porous membranes sintered at 1200°C.

Samples	Sample mass [g]	Total pore volume [cm^3/g]	Specific surface area [m^2/g]	Average pore diameter [μm]	Mode pore diameter [μm]	Median pore diameter [μm]
Non-doped	0.7396	0.198	2.20	0.36	0.63	0.60
LiF-doped	0.5364	0.477	0.85	2.24	5.07	4.89

Table 3. Density, porosity and filtration performance of porous membranes sintered at 1200°C.

	Density (g/cm^3)	Porosity (%)	Filtration rate (mL/min)	Turbidity (NTU)
Non-doped	1.38	58.3 [a]	2.26	1.46
LiF-doped	1.29	59.2 [b]	5.78	87.38

[a] Calculated from the theoretical density (3.31 g/cm^3) of 84 wt.% β''-alumina and 16 wt.% β-alumina.

[b] Calculated from the theoretical density (3.16 g/cm^3) of 84 wt.% β-alumina and 16 wt.% $NaAlO_2$.

Figure captions

Fig. 1 Filtration test setup (dead-end type).

Fig. 2 XRD patterns of (a) non-doped and (b) LiF-doped samples reactively sintered at 1100-1300°C.

Fig. 3 SEM micrographs of fracture surfaces: non-doped samples sintered at (a) 1100°C, (b) 1200°C, (c) 1300°C, and LiF-doped samples sintered at (d) 1100°C, (e) 1200°C, (f) 1300°C.

Fig. 4 Pore-size distributions determined by mercury porosimetry: (a) cumulative pore volume and (b) differential pore volume, dV/d(log D).

Fig. 5 Unfiltered water (894.4 NTU) and filtered water passing through non-doped (1.46 NTU) and LiF-doped (87.38 NTU) membranes.

Fig. 6 Optical microscopy images of surface morphology of porous membranes. Non-doped samples (a) before filtration, (b) upper-side after filtration and (c) bottom-side after filtration, and LiF-doped samples (d) before filtration, (e) upper-side after filtration and (f) bottom-side after filtration.

Fig. 7 Particle removal by card-house structures: (a) non-doped and (b) LiF-doped samples.

Fig. 8 Na_2O-Al_2O_3 phase-diagram [37].

Fig. 9 Filtration model in the card-house structure.

Figures

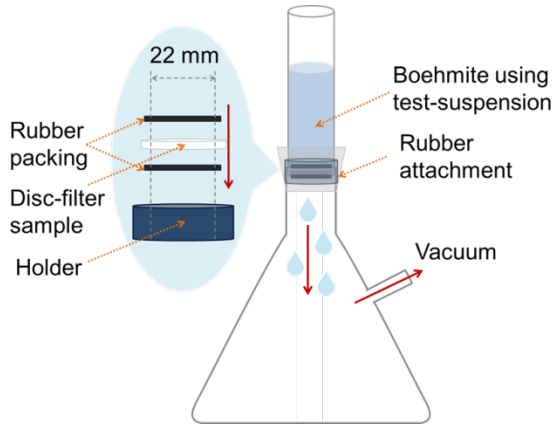

Fig. 1 Filtration test setup (dead-end type).

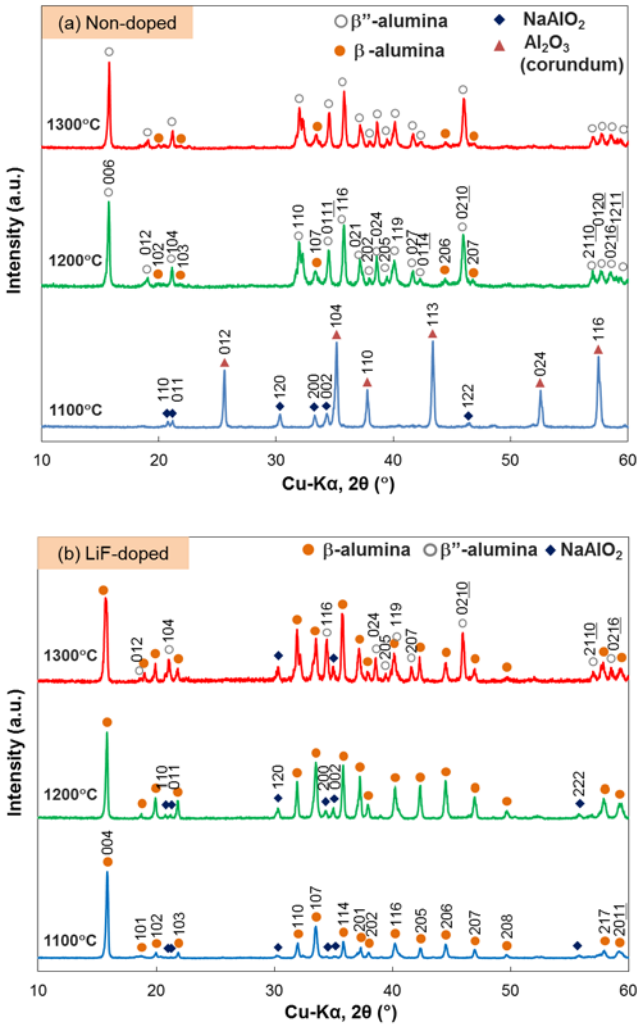

Fig. 2 XRD patterns of (a) non-doped and (b) LiF-doped samples reactively sintered at 1100-1300°C.

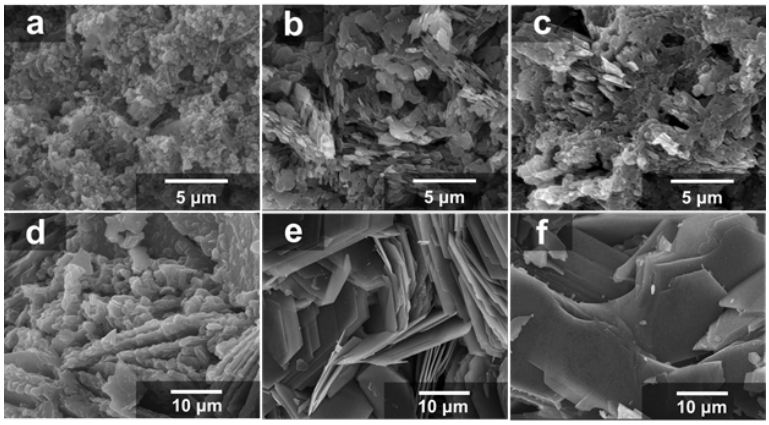

Fig. 3 SEM micrographs of fracture surfaces: non-doped samples sintered at (a) 1100°C, (b) 1200°C, (c) 1300°C, and LiF-doped samples sintered at (d) 1100°C, (e) 1200°C, (f) 1300°C.

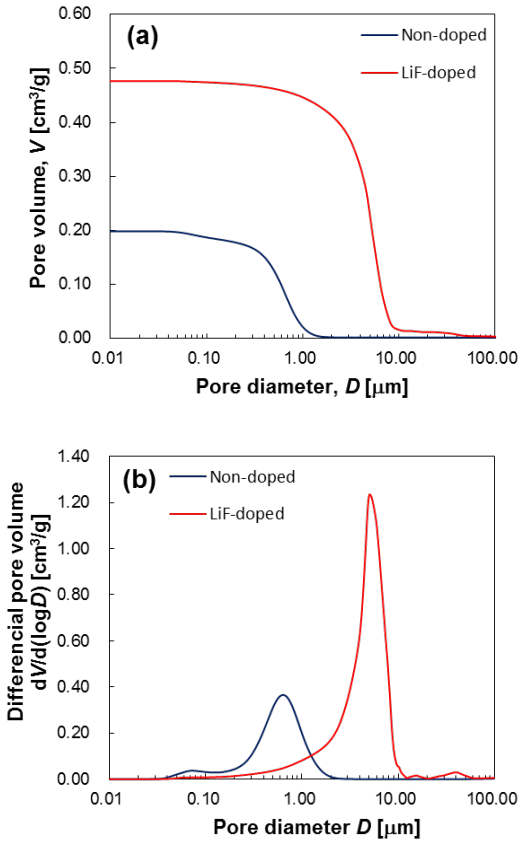

Fig. 4 Pore-size distributions determined by mercury porosimetry: (a) cumulative pore volume and (b) differential pore volume, d*V*/d(log *D*).

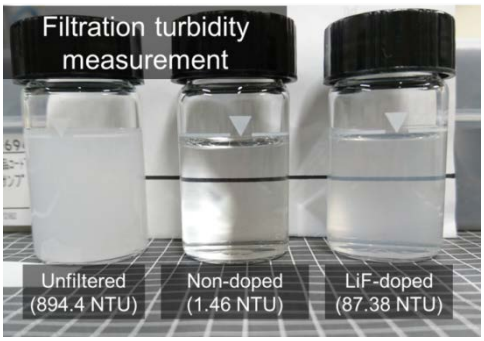

Fig. 5 Unfiltered water (894.4 NTU) and filtered water passing through non-doped (1.46 NTU) and LiF-doped (87.38 NTU) membranes.

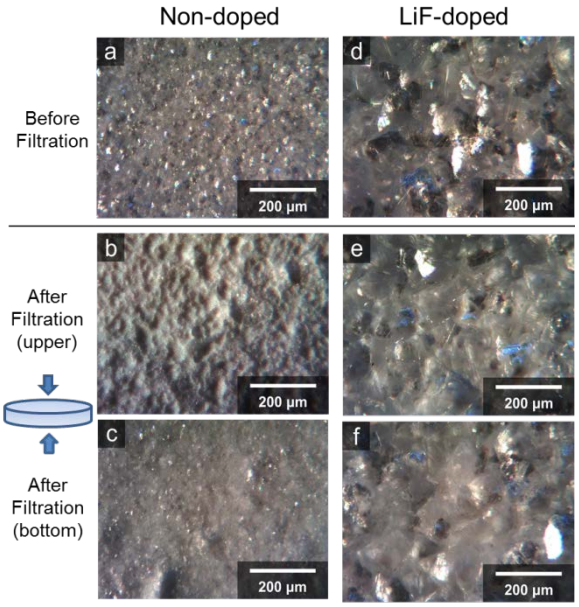

Fig. 6 Optical microscopy images of surface morphology of porous membranes. Non-doped samples (a) before filtration, (b) upper-side after filtration and (c) bottom-side after filtration, and LiF-doped samples (d) before filtration, (e) upper-side after filtration and (f) bottom-side after filtration.

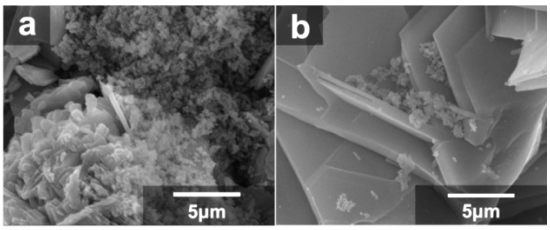

Fig. 7 Particle removal by card-house structures: (a) non-doped and (b) LiF-doped samples.

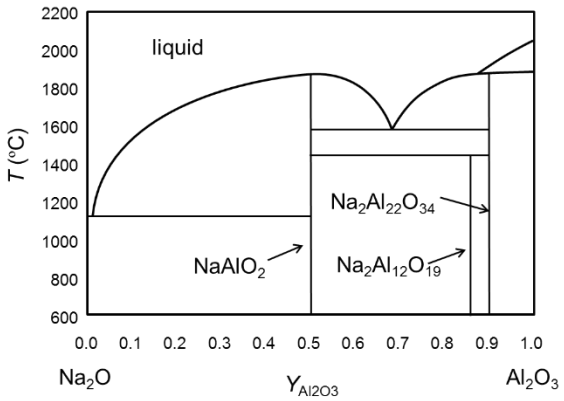

Fig. 8 Na_2O-Al_2O_3 phase-diagram [37].

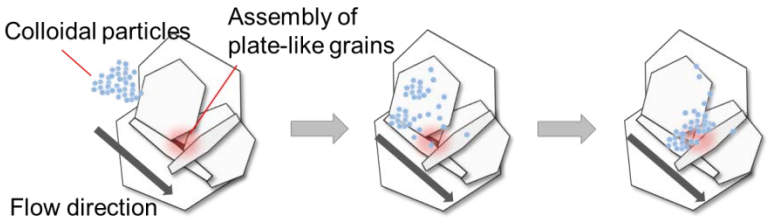

Fig. 9 Filtration model in the card-house structure.